van der Waals epitaxy and defect-charge manipulation of InSb islands on graphene-covered SiC(0001)

Zhihao Zhang, Hu Shi, Le Qin, Yan Liang, Wenhao Zhang ⬤, and Ying-Shuang Fu ⬤*

School of Physics and Wuhan National High Magnetic Field Center, Huazhong University of Science and Technology, Wuhan 430074, China

Indium antimonide has attracted extensive interest due to its optical and electronic applications, and functions as a constituent block in exploring Majorana physics. Here, through molecular-beam epitaxy, we achieve van der Waals epitaxy of high-quality InSb islands on graphene-covered SiC(0001) substrate. As characterized with spectroscopic imaging scanning tunneling microscopy (STM), the islands have tens of nanometers in thickness and a 2×2 surface reconstruction, exhibiting a narrow band gap of 0.315 ± 0.005 eV. Double concentric rings, whose diameters vary with the bias voltage of the STM tip, are observed in the spatially resolved conductance maps, which are explained as a charging process of solitary defects due to tip-induced band bending. Furthermore, high-temperature sample annealing induces a 3×3 surface reconstruction, which possesses a larger gap of 0.40 ± 0.01 eV. Our work demonstrates the feasibility of van der Waals epitaxy of the InSb traditional semiconductor and enriches the understanding of charging process in single defects.

I. INTRODUCTION

Indium antimonide (InSb) is a zinc-blende structured semiconductor belonging to the III–V family. InSb crystal has received a great deal of attention for decades because of its excellent optical and electronic properties. It has the smallest band gap of ∼0.235 eV amongst binary III–V compound semiconductors, and possesses a small effective mass of ∼0.015 m_e and an ultrahigh electron mobility of ∼77 000 cm^2/(V s) [1–4]. As such, InSb demonstrates wide applications in infrared detectors [5,6], high-speed transistors operating at low voltages [7], magnetic sensors [8], and, very recently, THz transport waveguides [9]. In addition, owing to its strong spin-orbit interaction [10,11], a large Landé *g* factor [12], and high mobility, InSb has functioned as an essential building block for constructing artificial topological superconductors, where Majorana modes emerge at the boundary of the superconductivity-proximitized InSb wires or films [13–15].

Those applications require the growth of high-quality InSb crystals. Various techniques, including molecular-beam epitaxy (MBE), liquid phase epitaxy, magnetron sputtering, and metalorganic vapor phase epitaxy, have been utilized for the epitaxial growth of InSb films [16–22]. The chosen substrates are limited to those with similar lattice constant of InSb to reduce the strain accumulated onto the epitaxial films. van der Waals (vdW) epitaxy, on the other hand, allows the growth of crystalline films with weak vdW interaction at the interfaces, where the lattice mismatch at the interface can be largely neglected. This greatly expands the available substrate for the grown films. Moreover, the epilayer can in principle be exfoliated from the substrate due to the weak interaction at the interface. However, the vdW epitaxy is conventionally applied for the growth of vdW crystals, and is rarely utilized for the growth of films with three-dimensional (3D) bulk structures.

Single atomic defects are one of the smallest structural units of a solid material. Manipulating the charge state of solitary defects in semiconductors not only enriches our understanding towards charge transfer at the single defect level, but also envisions to build functional devices that can reach the limit of miniaturization [23]. Scanning tunneling microscopy and spectroscopy (STM/STS) could characterize single defects in semiconductors owing to its high spatial and energy resolution [24]. The STM tip can also be used as a local electric gate to directly modify the electrostatic potential around single defects via tip-induced band bending (TIBB), rendering it an ideal tool for addressing and manipulating the charge state of single defects. While single charge states of solitary defects in semiconductors are relatively common, multiple charge states in individual charged impurities are rare.

In this study, we report the successful growth of high-quality InSb islands through vdW epitaxy with MBE on graphene-covered SiC(0001) substrate, which has the virtue of no constraint on the lattice match at the interface, in contrast to conventional growth. Utilizing STM/STS, we characterize the structural and electronic properties of the InSb islands. We observe subsurface charge dopants in InSb whose charge states can be manipulated with two successive charging events via TIBB, which are rarely observed in previous systems, enriches our understanding of charging process in individual defects.

II. METHODS

With MBE technique, we attempt to grow InSb on graphene-covered SiC(0001) substrate, because the graphene substrate is inert with weak vdW-type interaction with the

grown films. To obtain graphene, the SiC substrate was first degassed at 600°C for at least 3 h. Then it was flashed to 950°C for 2 min under Si flux, and it was subjected to five cycles similar to the flashing procedure. Subsequently, the Si source was turned off. And, the SiC was flashed to 1400°C for 10 min to desorb Si atoms and form double-layer graphene [25]. The high temperature was achieved by direct current heating and was monitored by an infrared pyrometer, which can measure temperatures ranging from 250 to 1400°C. Subsequently, the InSb island is grown by coevaporating In (purity 99.999%) and Sb (purity 99.95%) from a homemade tantalum boat and a Knudsen cell evaporator, respectively, with an approximate flux ratio of 1:8. The base MBE pressure is better than 8×10^{-10} Torr. The substrate temperature is kept suitably high enough to facilitate the island formation and desorption of excess Sb. However, a too high substrate temperature degrades the grown islands. The details on the effect of substrate temperature on the morphology of the grown InSb are depicted later. Such strategy has been used in the growth of GaAs [26], and numerous binary vdW compounds [27–29]. We found that InSb can desorb from graphene when the substrate temperature is increased to 600°C, leaving intact graphene. This excludes the possibility of reaction with the grown InSb, as well as avoiding the interfacial strain due to lattice mismatch.

STM/STS measurements were conducted in a custom-made cryogenic Unisoku STM (1200) system at 5 K [30]. The electrochemically etched W wire was used as the STM tip, which had been characterized on a standard Ag(111) multi-layer film grown on a Si(111) substrate before measurements. Both conductance spectra and maps were acquired by lock-in detection of the tunneling current with a modulation voltage at 983 Hz feeding into the sample bias.

III. RESULTS AND DISCUSSION

Bulk InSb belongs to a III–V semiconductor, whose crystal structure is of zinc-blende type with a lattice parameter of $a = 0.648$ nm [1]. Correspondingly, its in-plane lattice constant of the InSb(111) surface is $a_0 = a/\sqrt{2} = 0.458$ nm. The InSb(111) surface with In termination is called InSb(111)-A surface, while the InSb($\bar{1}\bar{1}\bar{1}$) surface with Sb termination is called InSb(111)-B surface. Previous studies have identified multiple reconstructions on the InSb(111) surface. Namely, the InSb(111)-B surface can exhibit (2×2), (3×3), and (3×1) reconstructions, while (2×2) and $(2\sqrt{3} \times 2\sqrt{3})$ $R30°$ reconstructions have been observed on the InSb(111)-A surface. Different surface reconstructions form depending on the preparation conditions such as growth temperature and the flux ratio of In to Sb [31–41].

Figure 1(a) shows a typical STM topographic image of as-grown InSb islands on a graphene substrate. The InSb islands exhibit triangle or hexagonal shapes with a spatial extension of tens to hundreds of nanometers and a thickness ranging from 6 to 20 nm. The spatial sizes of the InSb islands enlarge with increasing coverage, but cannot be grown into specific layers. During the growth, the temperature of the substrate was kept at 260°C, which is the optimal substrate temperature to grow atomically flat InSb surface with 2×2 surface reconstruction and minimal defects [Fig. 1(b)]. As
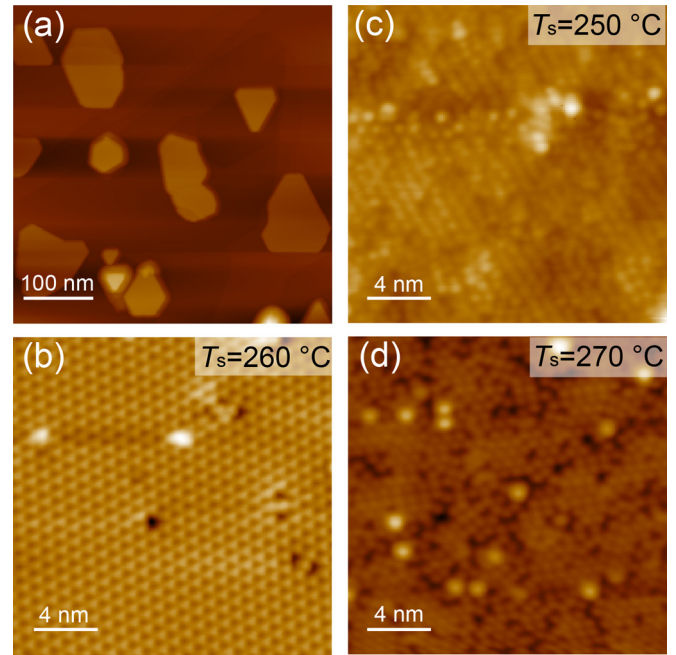
FIG. 1. (a) Large-scale STM image ($V_b = 2$ V, $I_t = 10$ pA) showing the topography of InSb islands grown on a graphene substrate. (b)–(d) Topography of the as-grown InSb islands with different substrate temperature T_s during growth. Substrate temperature: (b) $T_s = 260°$C (c) $T_s = 250°$C and (d) $T_s = 270°$C. Imaging conditions: (b) $V_b = 2$ V, $I_t = 10$ pA; (c) $V_b = 1$ V, $I_t = 10$ pA; and (d) $V_b = 2$ V, $I_t = 10$ pA.

shown in Figs. 1(c) and 1(d), when the substrate temperature is low (250°C), incomplete reconstruction, excessive defects, and rough surface will occur. When the substrate temperature is high (270°C), the defect density will increase prominently.

As is seen from the atomic resolution imaging of the InSb(111) surface in Fig. 2(a) and its fast Fourier transformation (FFT), the InSb(111) surface is atomically flat, exhibiting a triangular lattice. The lattice constant is determined as 0.905 $\pm$ 0.005 nm, which is twice the in-plane lattice constant of the bulk InSb(111) surface, i.e., a 2×2 reconstruction. The 2×2 reconstruction comes from Sb trimers that distribute on the outermost Sb layer of the InSb(111)-B surface [30,41], whose crystal structure is shown in Fig. 2(b). This agrees with our experimental growth condition of excess Sb. Figure 2(c) shows a zoomed-in image of the InSb island with a step on the surface. The step height is measured as 0.39 $\pm$ 0.01 nm from a traversing line profile across the step [Fig. 2(d)]. This apparent height is consistent with the theoretical interlayer spacing d of InSb(111), i.e., 0.374 nm.

Having identified the morphology and atomic structure of the InSb islands, we study their electronic structure by STS. Figure 3(a) shows a two-dimensional (2D) conductance plot of the InSb(111)-B-2 $\times$ 2 surface along a straight line in the inset of Fig. 3(b), and the corresponding averaged tunneling conductance spectrum is shown in Fig. 3(b). The thickness of the island where these spectra were taken is 8.6 $\pm$ 0.1 nm. The 2D dI/dV spectra, which are approximately uniform in real space, feature an evident narrow band gap of 315 $\pm$ 5 meV. The conduction- and valence-band edges are located
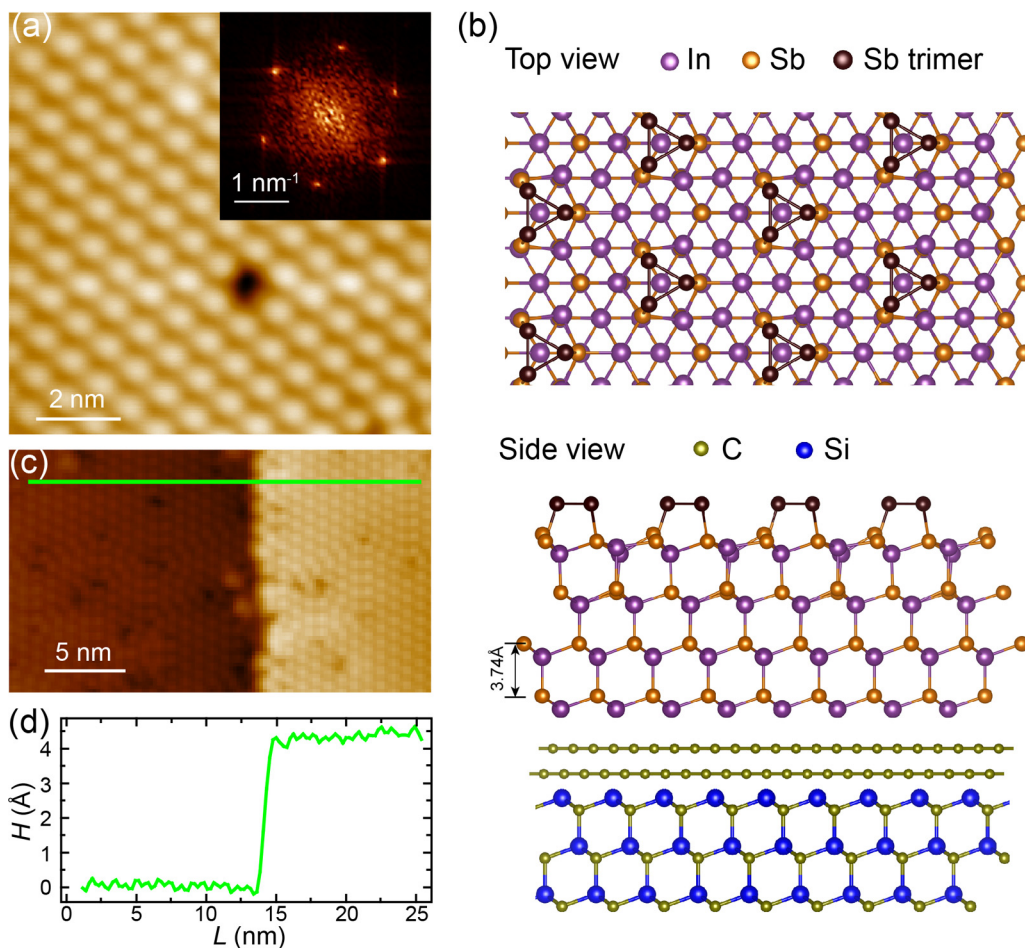
FIG. 2. Structure and morphology of InSb islands. (a) High-resolution STM image ($V_b = 2$ V, $I_t = 10$ pA) showing the atomic resolution 2×2 reconstruction of InSb(111)-B surface. Inset is the FFT image of (a). (b) Ball and stick model showing top and side view of the crystal structure of InSb islands with 2×2 reconstruction grown on graphene-covered SiC(0001). (c) Zoomed-in STM image ($V_b = 2$ V, $I_t = 10$ pA) showing the atomic structure of a step on the InSb surface. (d) Line profile across the step along the green line in (c).

at $+45$ and -270 meV, respectively. The measured band-gap size is larger than the bulk band gap of 235 meV measured in the previous works [1,2]. Such discrepancy is presumably due to fact that the measurement is of the 2×2 surface. As evidenced from the observed charging rings of solitary defects depicted later, TIBB effect exists in our case, which enlarges the measured gap size of insulators in STS experiments [42,43]. Therefore, the larger band gap of the 2×2 surface could also be, at least partially, caused by the TIBB effect. As shown in Figs. 3(a) and 3(b), there appear series of
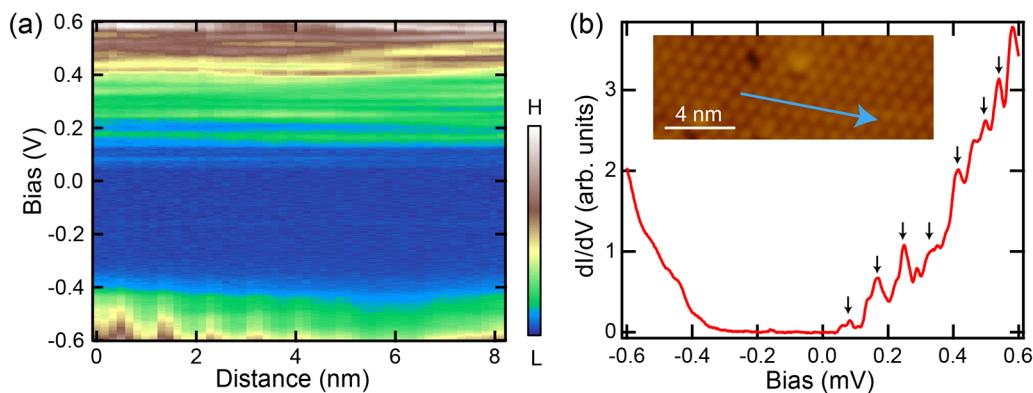
FIG. 3. Electronic structure of InSb islands. (a) 2D conductance plot obtained along the cyan arrow in the inset of (b). (b) An averaged tunneling spectrum of (a). Spectroscopic conditions: $V_b = 0.6$ V, $I_t = 100$ pA, $V_{mod} = 10$ mV. For clarity, the peaks in (b) are highlighted with black arrows.
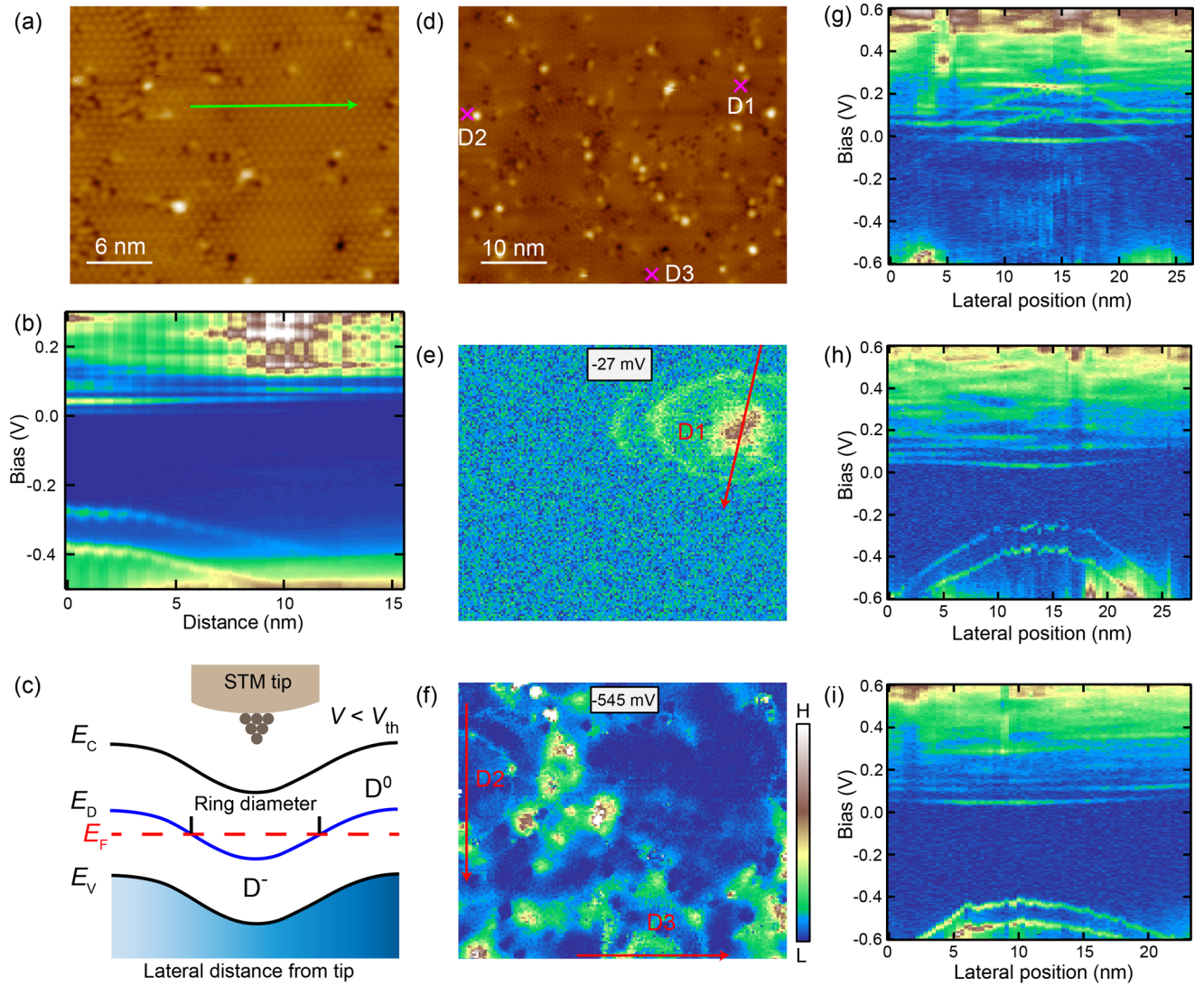
FIG. 4. TIBB effect on InSb islands. (a) STM topography image ($V_b = 2$ V, $I_t = 10$ pA) of the InSb(111)-B-2 × 2 surface. (b) 2D plot of tunneling spectra measured along the green arrow in the image of (a). Spectroscopic conditions: $V_b = 0.3$ V, $I_t = 10$ pA, and $V_{mod} = 10$ mV. (c) Schematic of the lateral TIBB on the sample below the STM tip, which shows the switch of charge-neutral D^0 to negative state D^-, when the sample bias (V) is lower than the threshold (V_{th}). (d) STM topography image ($V_b = 2$ V, $I_t = 10$ pA) on the same island with (a). (e), (f) Selective differential conductance mappings acquired over the same area of (d) at bias energies of −27 and −545 meV, respectively. Three concentric double rings that vary with bias energy are shown in the conductance mappings; they are marked as D1, D2, and D3, respectively. Spectroscopic conditions: $V_b = 0.6$ V, $I_t = 100$ pA, and $V_{mod} = 12$ mV. (g)–(i) 2D dI/dV cross sections along the red arrows in (e) and (f), and they passed through the concentric double rings D1, D2, and D3, respectively.

small peaks in the range of +50 to +600 meV, whose level spacings are approximately even. The level spacing is 80 ± 7 and 100 ± 10 meV for the InSb islands with thicknesses of 8 and 14 nm, respectively. For quantum-well states formed perpendicular to the film surface, the level spacing should decrease with increasing island thickness. This is in contrast to the observation, where the thinner InSb island has a smaller level spacing. This excludes the scenario of quantum-well states, and the associated trend with film thickness. The origin of these peaks is currently unclear and further study is needed.

Next, we examine the effect of defects on the electronic state. Unexpectedly, even though an area with no surface defects [Fig. 4(a)] is selected to acquire dI/dV spectra, there appears evident band shifting in the line spectra of Fig. 4(b).

Specifically, at the origin of the line spectra, two prominent peaks emerge within the band gap of InSb at −0.27 and −0.38 eV, respectively. Those two peaks gradually shift towards lower energy with the spectroscopic locations moving away from the origin. This suggests the existence of a subsurface defect at the origin. The spatial-dependent energy evolution of the two peaks can be explained as a charging process of the buried defect due to the TIBB effect [23,44], as schematically illustrated in Fig. 4(c). The electric field from the STM tip locally gates the bands of the semiconductor and induces band bending, leading to a shift of defect states relative to the Fermi level. Once the defect states pass through the Fermi level or band edges, the defect switches from a charge-neutral state D^0 to a negative charge state, engendering peaks
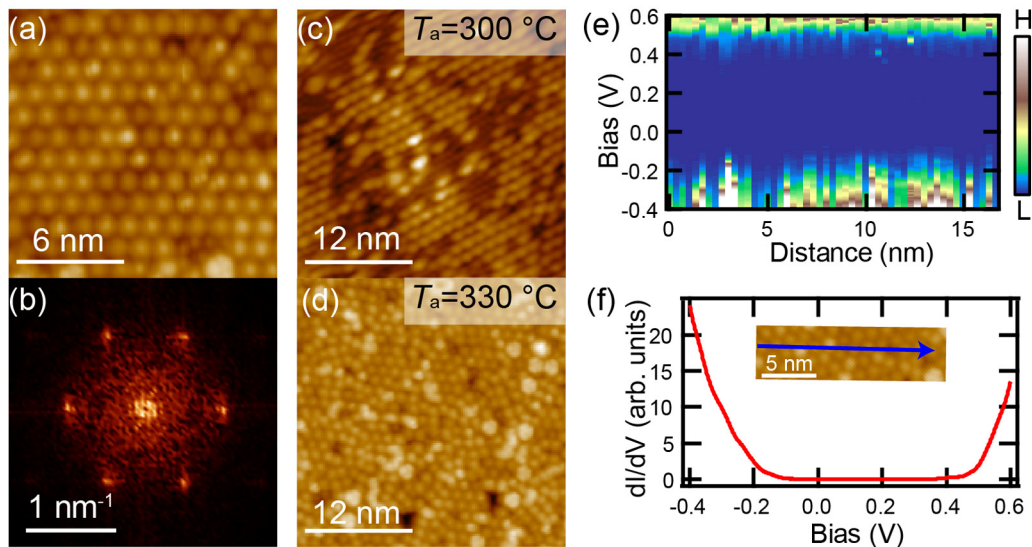
FIG. 5. 3×3 reconstruction on the InSb(111)B surface. (a) STM image ($V_b = 2$ V, $I_t = 10$ pA) of the atomic resolution reconstruction of InSb(111) surface; (b) FFT image of (a). (c), (d) Topographic images of the InSb islands after annealing at different annealing temperatures T_a for about 30 min. Annealing temperature: (c) $T_a = 300°$C (d) $T_a = 330°$C. Imaging conditions: (c) $V_b = 2$ V, $I_t = 10$ pA; (d) $V_b = 2$ V, $I_t = 10$ pA. (e) 2D plot of tunneling spectra measured along the blue arrow in the inset of (f). (f) Corresponding averaged tunneling spectrum of (e). Spectroscopic conditions: $V_b = 0.6$ V, $I_t = 100$ pA, and $V_{mod} = 10$ mV.

in STS, the locations and intensities of which are strongly sensitive to tip-defect distance or bias voltage [23,45,46]. Thus, the upward band bending upon approaching the charge center demonstrates the charged defect is an electron acceptor.

To substantiate the charging processes, we perform conductance mappings over the surface [Fig. 4(d)]. Although there are many atomic defects on the surface, selective *dI/dV* maps at −27 and −545 mV shown in Figs. 4(e) and 4(f) display three ringlike patterns. This further confirms that TIBB is not caused by these surface defects, but by the buried defects. The conductance rings appear as double rings that are concentric and nearly circular, whose spatial size varies with the bias voltage. This observation conforms to the double-peak feature in the line spectra of Fig. 4(b), and confirms the ringlike patterns are induced by the charging process. Notably, the emergence of a double-ring feature in the spectral mapping suggests two successive charging processes, i.e., a singly charged state D^- and a doubly charged state D^{2-}.

Similar ringlike structures were observed previously in charged impurities of multiple semiconductors both in the bulk [46–51] and in thin films [23,24,52–54]. However, most of those studies present single charge rings, demonstrating single charging events. The double charge rings, that are related to two successive charging events, are rarely observed. The only examples are the double rings in ZnO [44] and, very recently, five rings in Sn$_2$Bi [23].

As indicated in Figs. 4(e) and 4(f), the charge rings emerge at different energies, illustrating the onset voltages of these charging rings are different. Those charge defects are labeled as D1, D2, and D3, where the defect locations are marked with pink crosses in Fig. 4(d), as determined from the centers of the charge rings. Figures 4(g)–4(i) show line spectra that are taken across those defect centers. The line spectra all display parabolic-shaped energy evolution of the double charge peaks that bend upward in energy when approaching the charge

centers. The double parabolic spectra peaks correspond to the two consecutive charging events. The onsets of the parabolic-shaped bending peaks are measured as −0.24 and −0.35 eV for defect D2, which become −0.41 and −0.51 eV for defect D3. The distinct different onset charging energies suggests the defects are buried at different depths relative to the sample surface. More negative onset charging energy demonstrates the charge defects are deeper.

Remarkably, the onset charging energies of defect D1 are 0.22 and 0.12 eV, which are positive values. We propose the following scenario to understand the spectral features around D1. The positive onset charging energies imply the defect is already spontaneously charged with two additional electrons before the tip gating. The negatively charged defect locally induces band bending towards higher energy, shifting the valence-band edge above the Fermi level. The charge defect-induced band bending creates an electrostatic potential that confines electrons of the valence bands, which incurs the discrete energy around the Fermi level. The positive onset charging energies are associated with the thresholds of releasing the additional charges via the TIBB effect.

Finally, we discuss the modification of surface reconstruction and the associated electronic states. After being annealed at a temperature of 300–330°C for about 30 min, the InSb island surface presents a larger triangular lattice. From the atomic resolution imaging of InSb islands in Fig. 5(a) and its FFT [Fig. 5(b)], the lattice constant is estimated as 1.30 ± 0.05 nm, which is approximately equal to $3a_0 = 1.37$ nm [1], indicating that the InSb(111)-B surface is transformed into a 3 × 3 reconstruction. So far, the structural model of InSb(111)-B-3 × 3 reconstruction is still subject to discussion. The most accepted model was proposed by Wever *et al.* in 1994 based on x-ray diffraction and STM analysis. It was determined that the reconstructed surface is composed of three types of In-Sb hexamers: α-, β-, and γ rings [34]. This model is also reasonably

consistent with other experimental studies [33,37,38]. Due to the volatility of antimony, an InSb(111)-B-3 × 3 reconstruction obtained by annealing at high-temperature conditions is reasonable, which is also consistent with the previous results [37]. It is worth noting that a low-temperature annealing (300°C) may lead to partial 3 × 3 surface reconstruction [Fig. 5(c)], while a high-temperature annealing (330°C) may increase the surface defect density [Fig. 5(d)]. However, the electronic structure of the InSb(111)-B-3 × 3 surface reconstruction has not been studied. A 2D conductance plot [Fig. 5(e)] is obtained along the blue straight line in the inset of Fig. 5(f), whose corresponding averaged tunneling conductance spectrum is shown in Fig. 5(f). The spectra are relatively uniform in space, which features a semiconducting band gap of 0.40 ± 0.01 eV with the conduction- and valence-band edges located at +340 and −60 meV, respectively. Compared with the 2 × 2 reconstruction, the 3 × 3 surface reconstruction becomes significantly larger, providing a way to manipulate the electronic properties of semiconductors through surface reconstructions.

IV. SUMMARY

In summary, we achieved the vdW epitaxy of the III–V semiconductor InSb islands with atomically flat surfaces on a graphene-covered SiC(0001) substrate through the MBE method, and the spatial extension of InSb islands ranges from tens to hundreds of nanometers and with thicknesses ranging from 6 to 20 nm, whose surface expresses the typical InSb(111)-B-2 × 2 reconstruction. With STM/STS, we characterized the crystal structure and electronic band structure of InSb islands. The InSb islands with 2 × 2 reconstruction exhibit a narrow band gap of 0.315 ± 0.005 eV. Double concentric rings are observed in the spatially resolved *dI/dV* maps, which are ascribed to buried charge defects with two consecutive charging processes as manipulated via TIBB. Furthermore, a 3 × 3 reconstruction can be obtained by annealing the sample at a higher temperature, which possesses a larger gap of 0.40 ± 0.01 eV. Our finding identifies the feasibility of vdW epitaxy of a semiconductor with 3D atomic structure, which may be generalized to other materials. The manipulation of multiple charge states deepens our understanding of charging process in solitary defects [23,55].

[1] I. Vurgaftman, J. R. Meyer, and L. R. Ram-Mohan, Band parameters for III–V compound semiconductors and their alloys, J. Appl. Phys. **89**, 5815 (2001).

[2] C. L. Littler and D. G. Seiler, Temperature dependence of the energy gap of InSb using nonlinear optical techniques, Appl. Phys. Lett. **46**, 986 (1985).

[3] S. R. Plissard, D. R. Slapak, M. A. Verheijen, M. Hocevar, G. W. G. Immink, I. van Weperen, S. Nadj-Perge, S. M. Frolov, L. P. Kouwenhoven, and E. P. A. M. Bakkers, From InSb nanowires to Nanocubes: Looking for the sweet spot, Nano Lett. **12**, 1794 (2012).

[4] A. T. Vogel, J. de Boor, J. V. Wittemann, S. L. Mensah, P. Werner, and V. Schmidt, Fabrication of high-quality InSb nanowire arrays by chemical beam epitaxy, Cryst. Growth Des. **11**, 1896 (2011).

[5] E. G. Camargo, K. Ueno, T. Morishita, M. Sato, H. Endo, M. Kurihara, K. Ishibashi, and N. Kuze, High-sensitivity temperature measurement with miniaturized InSb Mid-IR sensor, IEEE Sens. J. **7**, 1335 (2007).

[6] C.-H. Kuo, J.-M. Wu, S.-J. Lin, and W.-C. Chang, High sensitivity of middle-wavelength infrared photodetectors based on an individual InSb nanowire, Nanoscale Res. Lett. **8**, 327 (2013).

[7] T. Ashley, A. R. Barnes, L. Buckle, S. Datta, A. B. Dean, M. T. Emeny, M. Fearn, D. G. Hayes, P. J. Wilding, R. Chau *et al.*, Novel InSb-based quantum well transistors for ultra-high speed, low power logic applications, in *Proceedings of the Seventh International Conference on Solid-State and Integrated Circuits Technology* (IEEE, New York, 2004), p. 2253.

[8] O. Kazakova, V. Panchal, J. Gallop, P. See, D. C. Cox, M. Spasova, and L. F. Cohen, Ultrasmall particle detection using a submicron Hall sensor, J. Appl. Phys. **107**, 09E708 (2010).

[9] Y. Ma, J. Zhou, J. Pištora, M. Eldlio, N. Nguyen-Huu, H. Maeda, Q. Wu, and M. Cada, Subwavelength InSb-based slot waveguides for THz transport: Concept and practical implementations, Sci. Rep. **6**, 38784 (2016).

[10] G. A. Khodaparast, R. E. Doezema, S. J. Chung, K. J. Goldammer, and M. B. Santos, Spectroscopy of Rashba spin splitting in InSb quantum wells, Phys. Rev. B **70**, 155322 (2004).

[11] T. Campos, P. E. Faria Junior, M. Gmitra, G. M. Sipahi, and J. Fabian, Spin-orbit coupling effects in zinc-blende InSb and wurtzite InAs nanowires: Realistic calculations with multiband **k • p** method, Phys. Rev. B **97**, 245402 (2018).

[12] K. L. Litvinenko, L. Nikzad, C. R. Pidgeon, J. Allam, L. F. Cohen, T. Ashley, M. Emeny, W. Zawadzki, and B. N. Murdin, Temperature dependence of the electron Landé *g* factor in InSb and GaAs, Phys. Rev. B **77**, 033204 (2008).

[13] V. Mourik, K. Zuo, S. M. Frolov, S. R. Plissard, E. P. A. M. Bakkers, and L. P. Kouwenhoven, Signatures of Majorana fermions in hybrid superconductor-semiconductor nanowire devices, Science **336**, 1003 (2012).

[14] J. Shabani, M. Kjaergaard, H. J. Suominen, Y. Kim, F. Nichele, K. Pakrouski, T. Stankevic, R. M. Lutchyn, P. Krogstrup, R. Feidenhans'l, S. Kraemer, C. Nayak, M. Troyer, C. M. Marcus, and C. J. Palmstrøm, Two-dimensional epitaxial superconductor-semiconductor heterostructures: A platform for topological superconducting networks, Phys. Rev. B **93**, 155402 (2016).

[15] R. M. Lutchyn, E. P. A. M. Bakkers, L. P. Kouwenhoven, P. Krogstrup, C. M. Marcus, and Y. Oreg, Majorana zero modes in superconductor–semiconductor heterostructures, Nat. Rev. Mater. **3**, 52 (2018).

[16] T. Zhang, S. K. Clowes, M. Debnath, A. Bennett, C. Roberts, J. J. Harris, R. A. Stradling, L. F. Cohena, T. Lyford, and P. F. Fewster, High-mobility thin InSb films grown by molecular beam epitaxy, Appl. Phys. Lett. **84**, 4463 (2004).

[17] H. T. Pham, S. F. Yoon, D. Boning, and S. Wicaksono, Molecular beam epitaxial growth of indium antimonide and its characterization, J. Vac. Sci. Technol. B **25**, 11 (2007).

[18] X.-M. Zhao, Y. Zhang, L.-J. Cui, M. Guan, B.-Q. Wang, Z.-P. Zhu, and Y.-P. Zeng, Growth and characterization of InSb thin films on GaAs (001) without any buffer layers by MBE, Chin. Phys. Lett. **34**, 076105 (2017).

[19] D. E. Holmes and G. S. Kamath, Growth characteristics of LPE InSb and InGaSb, J. Electron. Mater. **9**, 95 (1980).

[20] Z. C. Feng, C. Beckham, P. Schumaker, I. Ferguson, R. A. Stall, N. Schumaker, M. Povioski, and A. Whitley, Optical characterization and mapping of four INCH InSb epitaxial thin films grown on GaAs by turbo disk metalorganic chemical vapor deposition, MRS Proc. **450**, 61 (2011).

[21] M. Behet, B. Stoll, W. Brysch, and K. Heime, Growth of GaSb and InSb by low-pressure plasma MOVPE, J. Cryst. Growth **124**, 377 (1992).

[22] Y. Bu, M. C. Lin, A. D. Berry, and D. G. Hendershot, Low pressure chemical vapor deposition of InSb using neopentylstibine and trimethylindium, J. Vac. Sci. Technol. A **13**, 230 (1995).

[23] J. Gou, B. Xia, X. Wang, P. Cheng, A. T. S. Wee, W. Duan, Y. Xu, K. Wu, and L. Chen, Realizing quinary charge states of solitary defects in two-dimensional intermetallic semiconductor, Nat. Sci. Rev. **9**, nwab070 (2021).

[24] C.-L. Song, Y.-P. Jiang, Y.-L. Wang, Z. Li, L. Wang, K. He, X. Chen, X.-C. Ma, and Q.-K. Xue, Gating the charge state of single Fe dopants in the topological insulator Bi_2Se_3 with a scanning tunneling microscope, Phys. Rev. B **86**, 045441 (2012).

[25] X. Yang, J.-J. Xian, G. Li, N. Nagaosa, W.-H. Zhang, L. Qin, Z.-M. Zhang, J.-T. Lü, and Y.-S. Fu, Possible Phason-Polaron Effect on Purely One-Dimensional Charge Order of Mo_6Se_6 Nanowires, Phys. Rev. X **10**, 031061 (2020).

[26] Q.-K. Xue, T. Hashizume, and T. Sakurai, Scanning tunneling microscopy of III-V compound semiconductor (001) surfaces, Prog. Surf. Sci. **56**, 1 (1997).

[27] Y. Zhang, T.-R. Chang, B. Zhou, Y.-T. Cui, H. Yan, Z. Liu, F. Schmitt, Z. Hussain, A. Bansil, Z.-X. Shen *et al.*, Direct observation of the transition from indirect to direct bandgap in atomically thin epitaxial $MoSe_2$, Nat. Nanotechnol. **9**, 111 (2014).

[28] L. Peng, J. Zhao, M. Cai, G.-Y. Hua, Z.-Y. Liu, H.-N. Xia, Y. Yuan, W.-H. Zhang, G. Xu, L.-X. Zhao, Z.-W. Zhu, T. Xiang, and Y.-S. Fu, Mott phase in a van der Waals transition-metal halide at single layer limit, Phys. Rev. Research **2**, 023264 (2020).

[29] J.-J. Xian, C. Wang, J.-H. Nie, R. Li, M. Han, J. Lin, W.-H. Zhang, Z. Xia, W. Ji, Y.-S. Fu *et al.*, Spin mapping of intralayer antiferromagnetism and field-induced spin reorientation in monolayer $CrTe_2$, Nat. Commun. **13**, 257 (2022).

[30] L. Qin, Z. H. Zhang, Z. Y. Jiang, K. Fan, W. H. Zhang, Q. Y. Tang, H. N. Xia, D. West, S. B. Zhang, Y. S. Fu *et al.*, Realization of AlSb in the double-layer honeycomb structure: a robust class of two-dimensional material, ACS Nano **15**, 8184 (2021).

[31] T. Nakada, T. Ikeda, M. Yata, and T. Osaka, In-situ observation of the polar InSb(111) reconstructed surface by ultra high vacuum reflection electron microscopy, Surf. Sci. **222**, L825 (1989).

[32] T. Nakada and T. Osaka, Sb Trimer Structure of the InSb(111)B-(2 × 2) Surface as Determined by Transmission Electron Diffraction, Phys. Rev. Lett. **67**, 2834 (1991).

[33] L. Ö. Olsson, J. Kanski, L. Ilver, C. B. M. Andersson, M. Björkqvist, M. Göthelid, U. O. Karlsson, and M. C. Håkansson, Surface electronic structure of InSb(111)3 × 3 studied by angle-resolved photoelectron spectroscopy and scanning tunneling microscopy, Phys. Rev. B **50**, 18172 (1994).

[34] J. Wever, H. L. Meyerheim, W. Moritz, V. Jahns, D. Wolf, H. Schulz, L. Seehofer, and R. L. Johnson, A new type of reconstruction on the InSb(111) surface determined by grazing incidence X-ray diffraction, Surf. Sci. **321**, L225 (1994).

[35] S. Cho, Y.-H. Um, Y. Kim, G. K. L. Wong, J. B. Ketterson, and J.-I. Hong, Bi epitaxy on polar InSb(111)*A*/*B* faces, J. Vac. Sci. Technol. A **20**, 1191 (2002).

[36] M. Björkqvist, M. Göthelid, L. Ö. Olsson, J. Kanski, and U. O. Karlsson, InSb(111)3 × 1: New surface reconstruction, J. Vac. Sci. Technol. B **14**, 957 (1996).

[37] J. Mäkelä, Z. S. Jahanshah Rad, J.-P. Lehtiö, M. Kuzmin, M. P. J. Punkkinen, P. Laukkanen, and K. Kokko, Crystalline and oxide phases revealed and formed on InSb(111)B, Sci. Rep. **8**, 14382 (2018).

[38] C. Liu, Y. Zhou, G. Wang, Y. Yin, C. Li, H. Huang, D. Guan, Y. Li, S. Wang, H. Zheng *et al.*, Sierpiński Structure and Electronic Topology in Bi Thin Films on InSb(111)B Surfaces, Phys. Rev. Lett. **126**, 176102 (2021).

[39] A. J. Noreika, M. H. Francombe, and C. E. C. Wood, Growth of Sb and InSb by molecular-beam epitaxy, J. Appl. Phys. **52**, 7416 (1981).

[40] M. Nishizawa, T. Eguchi, S.-i. Omoto, and T. Osaka, STM study of the InSb(111)A − (2 × 6) surface, Appl. Surf. Sci. **121/122**, 204 (1997).

[41] T. Eguchi, T. Miura, S.-P. Cho, T. Kadohira, N. Naruse, and T. Osaka, Structures and electronic states of the InSb{111}A, B − (2 × 2) surfaces, Surf. Sci. **514**, 343 (2002).

[42] R. M. Feenstra and J. A. Stroscio, Tunneling spectroscopy of the GaAs(110) surface, J. Vac. Sci. Technol. B **5**, 923 (1987).

[43] R. M. Feenstra, Tunneling spectroscopy of the (110) surface of direct-gap III-V semiconductors, Phys. Rev. B **50**, 4561 (1994).

[44] H. Zheng, J. Kröger, and R. Berndt, Spectroscopy of Single Donors at ZnO(0001) Surfaces, Phys. Rev. Lett. **108**, 076801 (2012).

[45] B. Kiraly, A. N. Rudenko, W. M. J. van Weerdenburg, D. Wegner, M. I. Katsnelson, and A. A. Khajetoorians, An orbitally derived single-atom magnetic memory, Nat. Commun. **9**, 3904 (2018).

[46] G. D. Nguyen, L. Liang, Q. Zou, M. Fu, A. D. Oyedele, B. G. Sumpter, Z. Liu, Z. Gai, K. Xiao, and A.-P. Li, 3D Imaging and Manipulation of Subsurface Selenium Vacancies in $PdSe_2$, Phys. Rev. Lett. **121**, 086101 (2018).

[47] D. Eom, E. Seo, and J.-Y. Koo, Surface-sensitive measurement of dielectric screening via atom and electron manipulations, Phys. Rev. B **94**, 195308 (2016).

[48] K. Teichmann, M. Wenderoth, S. Loth, R. G. Ulbrich, J. K. Garleff, A. P. Wijnheijmer, and P. M. Koenraad, Controlled

Charge Switching on a Single Donor with a Scanning Tunneling Microscope, Phys. Rev. Lett. **101**, 076103 (2008).

[49] F. Marczinowski, J. Wiebe, J. M. Tang, M. E. Flatté, F. Meier, M. Morgenstern, and R. Wiesendanger, Local Electronic Structure near Mn Acceptors in InAs: Surface-Induced Symmetry Breaking and Coupling to Host States, Phys. Rev. Lett. **99**, 157202 (2007).

[50] I. Battisti, V. Fedoseev, K. M. Bastiaans, A. de la Torre, R. S. Perry, F. Baumberger, and M. P. Allan, Poor electronic screening in lightly doped Mott insulators observed with scanning tunneling microscopy, Phys. Rev. B **95**, 235141 (2017).

[51] H. Zheng, A. Weismann, and R. Berndt, Manipulation of Subsurface Donors in ZnO, Phys. Rev. Lett. **110**, 226101 (2013).

[52] N. A. Pradhan, N. Liu, C. Silien, and W. Ho, Atomic Scale Conductance Induced by Single Impurity Charging, Phys. Rev. Lett. **94**, 076801 (2005).

[53] V. W. Brar, R. Decker, H.-M. Solowan, Y. Wang, L. Maserati, K. T. Chan, H. Lee, S. G. Louie, M. L. Cohen, M. F. Crommie *et al.*, Gate-controlled ionization and screening of cobalt adatoms on a graphene surface, Nature Phys. **7**, 43 (2011).

[54] Z. Qiu, H. Fang, A. Carvalho, A. S. Rodin, Y. Liu, S. J. R. Tan, M. Telychko, P. Lv, A. H. Castro Neto, J. Lu *et al.*, Resolving the spatial structures of bound hole states in black phosphorus, Nano Lett. **17**, 6935 (2017).

[55] P. M. Koenraad and M. E. Flatté, Single dopants in semiconductors, Nat. Mater. **10**, 91 (2011).